# Hyperfine-resolved 3.4-$\mu$m spectroscopy of $CH_3I$ with a widely tunable difference frequency generation source and a cavity-enhanced cell: A case study of a local Coriolis interaction between the $v_1 = 1$ and $(v_2, v_6^l) = (1, 2^2)$ states

Sho Okubo, Hirotaka Nakayama, and Hiroyuki Sasada

*Department of Physics, Faculty of Science and Technology, Keio University, 3-14-1 Hiyoshi, Kohoku-ku, Yokohama 223-8522, Japan and SENTAN, Japan Science and Technology Agency, Sanbancho 5, Chiyoda ku, Tokyo 102-0075, Japan*

(Received 30 October 2010; published 7 January 2011)

Saturated absorption spectra of the $\nu_1$ fundamental band of $CH_3I$ are recorded with a cavity-enhanced cell and a tunable difference frequency generation source having an 86-$cm^{-1}$ range. The recorded spectral lines are 250 kHz wide, and most of them are resolved into the individual hyperfine components. The Coriolis interaction between the $v_1 = 1$ and $(v_2, v_6^l) = (1, 2^2)$ states locally perturbing the hyperfine structures is analyzed to yield the Coriolis and hyperfine coupling constants with uncertainties similar to those in typical microwave spectroscopy. The spectrometer has demonstrated the potential for precisely determining the energy structure in the vibrational excited states.

DOI: 10.1103/PhysRevA.83.012505 PACS number(s): 33.20.Ea, 33.15.Pw, 33.15.Mt, 07.57.Ty

## I. INTRODUCTION

Infrared molecular spectroscopy has provided fundamental information on vibration-rotation structures and has contributed to the development of various fields such as molecular physics, physical chemistry, environmental science, diagnostics, and astronomy. Infrared spectra are usually recorded with a Fourier transform infrared (FTIR) spectrometer in Doppler-limited resolution. Saturated absorption spectroscopy is able to enhance the spectral resolution by $10^2$ to $10^4$ times that with the FTIR spectrometer when intense continuous-wave radiation sources with a narrow linewidth are available [1]. Because diode and solid-state lasers in the visible and near-infrared regions have developed remarkably, atomic electronic transitions are readily observed in sub-Doppler resolution. In contrast, molecular vibration-rotation transitions have been unexplored in sub-Doppler resolution, due to the lack of convenient radiation sources in the mid-infrared region. Molecular spectroscopy additionally requires wide tunability of radiation sources because a molecular vibrational band typically spreads over a few hundred $cm^{-1}$. The 10-$\mu$m region is exceptional, where $CO_2$ and $N_2O$ lasers provide plenty of oscillating lines for sub-Doppler resolution spectroscopy [2,3].

Difference frequency generation (DFG) provides mid-infrared radiation using advanced near-infrared lasers. We developed a 3.4-$\mu$m spectrometer with a DFG source consisting of an efficient waveguide-type periodically poled lithium niobate (PPLN) as a wavelength conversion element [4], a 1.064-$\mu$m Nd:YAG laser as a pump source, and a 1.55-$\mu$m distributed feedback (DFB) laser as a signal source [5]. The 3-$\mu$m region is particularly important for molecular spectroscopy because there are the fundamental vibrational bands of the C-H, N-H, and O-H stretching modes. Maddaloni and his co-workers observed 3.3-$\mu$m sub-Doppler resolution spectrum of methane using a DFG source [6]. Our spectrometer was also applied to sub-Doppler resolution spectroscopy of methane, and the transition frequencies were determined in a relative uncertainty of $10^{-10}$ with a fiber-laser-based frequency comb [7].

In the present work, the spectrometer is combined with an optical cavity absorption cell (cavity-enhanced cell) to enhance the optical field strength and the sensitivity. In addition, the 1.55-$\mu$m DFB laser is replaced with an external-cavity laser diode (ECLD). The tunable range of the signal source is thereby extended from 10 to 957 $cm^{-1}$, but that of the DFG source is limited to 86 $cm^{-1}$ by the temperature tuning range of the PPLN for phase matching. Because the spectral line of ECLD is broad and fluctuates in frequency in comparison with the DFB laser, we stabilize the ECLD frequency at one of the cavity modes of the cavity-enhanced cell using the Pound-Drever-Hall (PDH) method [8,9]. The spectrometer tunability and the sensitivity are thus improved without appreciable loss of the spectral resolution.

Here we demonstrate the performance of the spectrometer by recording the sub-Doppler resolution spectrum of the $\nu_1$ band of $CH_3I$. It is an excellent benchmark because infrared spectra have been extensively investigated in Doppler-limited resolution [10–12], and an electronic quadrupole hyperfine structure has also been studied in the vibrational ground state and some thermally populated vibrational excited states in microwave spectroscopy [13–16]. Microwave radio-frequency (rf) double-resonance spectroscopy was also employed in the vibrational ground state [17]. In the $\nu_6$ band, infrared rf [18,19] and infrared mm-wave [20] double-resonance spectroscopy were performed using the 10-$\mu$m $CO_2$ and $N_2O$ lasers; in the $2\nu_4$ band, infrared rf double-resonance spectroscopy was carried out using a 1.65-$\mu$m diode laser [21]. However, the $\nu_1$ band has not yet been recorded in sub-Doppler resolution, and neither microwave nor rf spectroscopy has been reported in the $v_1 = 1$ state.

## II. EXPERIMENT

Figure 1 schematically depicts the sub-Doppler-resolution spectrometer. A DFG source consists of a 1.55-$\mu$m ECLD as a signal source, a 1.06-$\mu$m Nd:YAG laser as a pump source, and a waveguide-type PPLN. The signal wave is boosted by a fiber amplifier, and combined with the pump wave by a fiber coupler. The combined waves are then fed into the PPLN module through a pigtail fiber. The temperature of the PPLN is controlled by a Peltier element in the module to accomplish phase matching, which limits the tuning range of the DFG

 

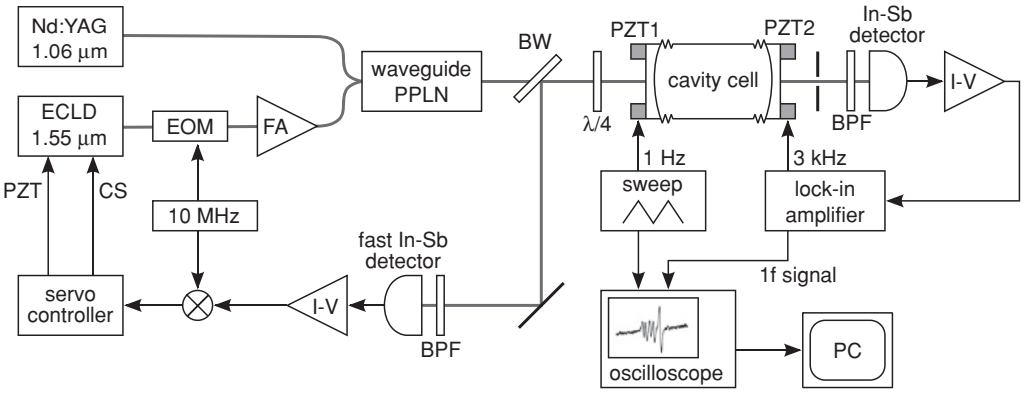


FIG. 1. Schematic of the experimental setup. ECLD, external-cavity laser diode; EOM, electro-optic modulator; FA, fiber amplifier; PPLN, periodically poled lithium niobate; BW, Brewster's window; $\lambda/4$, quarter-wave plate; PZT, piezoelectric transducer; BPF, bandpass filter; *I-V*, current to voltage converter; CS, current source.

source from 2885 to 2971 $cm^{-1}$. The generated 3.4-$\mu$m idler wave has a typical power level of 300 $\mu$W for the signal and pump power levels of 70 and 40 mW, corresponding to the conversion efficiency of about 10%/W.

A cavity-enhanced cell has two identical concave mirrors with a 99.0% power reflectivity at 3.4 $\mu$m and a radius of curvature of 2 m. They are optical windows at the same time, separated by 23.6 cm. The free spectral range of 636.16 MHz and the fringe width of 2.1 MHz (full width at half maximum), corresponding to a finesse of 303, are measured by generating a series of sidebands using a 1.55-$\mu$m inline electro-optic modulator (EOM). The effective absorption length increases by 198-fold, and the optical field strength at the antinodes is enhanced by 20 times. The mirrors are fixed between a ring-shaped piezoelectric transducer (PZT) and a bellows, and the cavity length is varied by applying voltage to the PZTs. The cavity-enhanced cell is filled with 1.9-Pa $CH_3I$. The idler wave transmitted through the cavity-enhanced cell and a 3.4-$\mu$m bandpass filter is detected by a liquid-nitrogen-cooled InSb detector. The photocurrent signal is converted into a voltage signal.

The frequency of the idler wave is servo locked to one of the longitudinal modes of the cavity-enhanced cell by the PDH method. The signal wave from the ECLD is phase modulated by the inline EOM at 10 MHz, which simultaneously frequency modulates the idler wave. The idler wave reflected from the cavity-enhanced cell is extracted by a silicon Brewster's plate and a quarter-wave plate in front of the cavity-enhanced cell, and detected by another liquid-nitrogen-cooled InSb detector with a bandwidth of 30 MHz. The photocurrent is converted to a voltage signal, which is demodulated by a double-balanced mixer at 10 MHz. Of the resultant error signal, the frequency component lower than 1.4 Hz is fed back to a PZT driving the grating of the ECLD through a proportional integration controller, and the higher frequency component is fed to the injection current of the ECLD. The resonant frequency of the cavity modes is swept by applying a 1-Hz triangle voltage to the PZT1 of the cavity-enhanced cell, while the idler frequency follows the cavity resonance through the servo control.

To reduce the background of the transmission signal caused by the Doppler-broadened spectral line, the cavity length is modulated by applying a 3-kHz sinusoidal voltage with a peak-to-peak modulation depth of 200 kHz to the PZT2 of the cavity-enhanced cell. The frequency of the idler wave tightly follows the 3-kHz modulation because of the 250-kHz servo bandwidth of the PDH method. The detected transmission signal is demodulated at 3 kHz (1*f* detection) by a lock-in amplifier at a time constant of 1.25 ms and recorded with a digital oscilloscope after averaging the 1*f* signal during 4–16 upward frequency sweeps, and the 1*f* signal is stored by a PC. The signal to noise (*S*/*N*) ratio is mainly determined by the saturation of the electronics, fluctuation in the idler power level, and a small oscillation of the servo signal for frequency stabilization. High idler power increases the amplitude of the Lamb dip, but at the same time saturates the 1*f* signal level. Therefore we reduce the idler power incident to the detector by putting a pinhole between the cavity-enhanced cell and the detector.

## III. RESULTS

Figure 2 plots the observed spectrum of the $\nu_1$ $P(J = 23, K = 5)$ transition. The peak absorbance of the

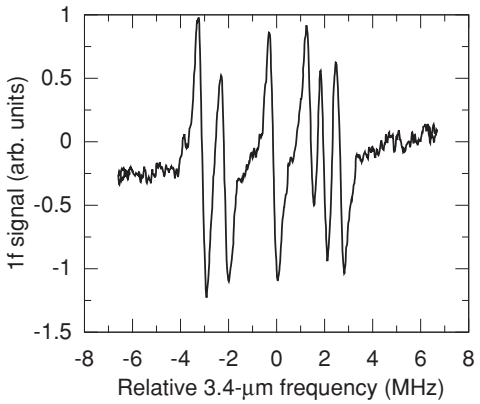


FIG. 2. Observed spectrum of the $\nu_1$ $P(23,5)$ transition. The hyperfine components are $(F'' \rightarrow F') = (\frac{51}{2} \rightarrow \frac{49}{2})$, $(\frac{41}{2} \rightarrow \frac{39}{2})$, $(\frac{49}{2} \rightarrow \frac{47}{2})$, $(\frac{43}{2} \rightarrow \frac{41}{2})$, $(\frac{47}{2} \rightarrow \frac{45}{2})$, and $(\frac{45}{2} \rightarrow \frac{43}{2})$ in the order to the higher frequency, where $F''$ and $F'$ are the total angular momentum quantum numbers of the vibrational ground and $\nu_1 = 1$ states, respectively.

TABLE I. Observed $P$-branch transitions of the $\nu_1$ band and ${}^P P$-branch transitions of the $\nu_2 + 2\nu_6$ band.

| $\nu_1\ P(J,K)$ | | | | $\nu_2 + 2\nu_6^{2\,P}\ P(J,K)$ |
|---|---|---|---|---|
| (17,7) | (17,9) | (18,8) | (19,6) | (21,4) |
| (19,8) | (20,4) | (20,7) | (21,3) | (22,4) |
| (21,4) | (21,6) | (22,4) | (22,5) | (23,4) |
| (22,6) | (23,4) | (23,5) | (24,2) | (24,4) |
| (24,4) | (25,0) | (25,1) | (25,2) | (25,4) |
| (26,4) | (27,4) | (28,2) | | (26,4) |

Doppler-broadened linear absorption line is 28%, and the Lamb dip is typically 1% deep relative to it. The electric quadrupole interaction of the iodine nucleus, whose nuclear spin $I$ is 5/2, splits the vibration-rotation level into six hyperfine sublevels of $\boldsymbol{F} = \boldsymbol{I} + \boldsymbol{J}$. In Fig. 2, six intense hyperfine components ($\Delta F = \Delta J$) of the transition are completely resolved. Assuming that the observed spectral line is the first derivative of the Lorentz profile, the linewidths are in the range of 250–290 kHz [HWHM (half width at half maximum)]. The horizontal axis indicates the 3.4-$\mu$m frequency converted from the voltage applied to the PZT1 of the cavity-enhanced cell. To determine the conversion factor, the idler wave is frequency modulated by the inline EOM at 10 MHz, and the 10-MHz-spaced sidebands transmitted through the cavity-enhanced cell without any servo controls are recorded while applying sawtooth voltage to the PZT1. The relative accuracy of the frequency scale is better than 10%. In this procedure, the ECLD is replaced with the DFB laser because it has better free-running frequency stability than the ECLD.

We have observed 174 hyperfine components of 23 vibration-rotation transitions of the $\nu_1$ band and six transitions of the $\nu_2 + 2$ band of $CH_3I$ in sub-Doppler resolution, and they are listed in Table I. Assignment is made according to the previous FTIR measurements [10–12]. The observed transitions of the $\nu_2 + 2\nu_6$ band borrow intensity from the $\nu_1$ band through the local Coriolis interaction, even though the combination bands are usually much weaker than the fundamental bands. The frequency intervals between the hyperfine components are measured; those for the $\nu_1$ $P(23,4)$ transition are listed in Table II.

## IV. ANALYSIS

The nuclear electric quadrupole interaction energy for symmetric top molecules such as $CH_3I$ is represented as

$$E_v^Q(I,J,K,F) = (eqQ)_v \left[\frac{3K^2}{J(J+1)} - 1\right] f(I,J,F), \quad (1)$$

where

$$f(I,J,F) = \frac{\frac{3}{4}C(C+1) - I(I+1)J(J+1)}{2I\,(2I-1)\,(2J-1)(2J+3)} \quad (2)$$

is the Casimir function, $C = F(F+1) - I(I+1) - J(J+1)$, and $(eqQ)_v$ is a quadrupole coupling constant [22]. The subscript $v$ represents a vibrational state. We will present the molecular constants with the dimension of energy in frequency units. For the vibrational ground state, Carocci and co-workers accurately yielded $(eqQ)_G = -1934.1306(51)$ MHz by combining the measurements in the infrared, microwave, and rf regions [23]. The number in the parentheses is one standard deviation in the unit of the last digit of the value. For the $v_1 = 1$ state, Hall and colleague reported $(eqQ)_{v_1=1} = 1937.06(3)$ MHz by means of high-resolution saturated absorption spectroscopy with a 3.39-$\mu$m He-Ne laser [24]. However, these constants are not able to account for the hyperfine-resolved spectral lines associated with the $(v_1 = 1, J, K = 4, F)$ levels because these levels coincide in energy with the $(v_2 = 1, v_6^l = 2^2, J, K = 3, F)$ levels and thereby both levels are strongly perturbed by the Coriolis interaction. Figure 3(a) presents the energy-level diagram at $J = 23$ and the energy coincidence between them. The nonperturbed energy levels cross each other around $J = 23$ as shown in Fig. 3(b). This local Coriolis resonance induces appreciable energy shifts of the vibration-rotation levels, which was already reported from Doppler-limited infrared measurements [11,12]. Figure 4 depicts the observed spectrum of the $\nu_1$ $P(24,3)$ and $P(23,4)$ transitions, which overlap within Doppler-limited resolution because the energy of the $(v_1 = 1, J = 22, K = 4)$ level is shifted $-4.5$ GHz by the Coriolis interaction. The bars indicate the transition frequency of the hyperfine components calculated from the hyperfine coupling constant of the vibrational ground and $v_1 = 1$ states [23,24], and their height represents the relative intensity of the hyperfine components [22]. The observed hyperfine structure agrees with the bars for the $\nu_1$ $P(24,3)$ transitions,

TABLE II. Fit of the hyperfine splitting of the $\nu_1$ P(23,4) transition. The transition frequency $f$ depends on the total angular momentum of the lower level $F''$ and the upper levels $F'$, respectively. The values in the column "calculated" are derived from $(eqQ)_G$ and $(eqQ)_{v_1=1}$ in Refs. [23] and [24], and those in the column "recalculated" are obtained from $(eqQ)_G$ in Ref. [23] and the determined constants in Table III.

| | Transition frequency interval: $\left[f(F'' \to F') - f\left(F'' = \frac{41}{2} \to F' = \frac{39}{2}\right)\right]$ / MHz | | | |
|---|---|---|---|---|
| $F'' \to F'$ | Measured | Calculated | Recalculated | (Measured)-(Recalculated) |
| $\frac{43}{2} \to \frac{41}{2}$ | −2.68 | 2.36 | −2.81 | 0.13 |
| $\frac{45}{2} \to \frac{43}{2}$ | −5.18 | 2.83 | −5.34 | 0.16 |
| $\frac{47}{2} \to \frac{45}{2}$ | −6.55 | 1.99 | −6.66 | 0.11 |
| $\frac{49}{2} \to \frac{47}{2}$ | −5.68 | 0.47 | −5.79 | 0.11 |
| $\frac{51}{2} \to \frac{49}{2}$ | −1.63 | −1.05 | −1.65 | 0.02 |

whereas agreement is substantially poor for the $\nu_1$ $P(23,4)$ transition in Fig. 4 and Table II.

To take into account of the Coriolis interaction, we consider a $2 \times 2$ Hamiltonian matrix for the specific $F$ value as

$$\begin{pmatrix} E(v_1=1,J,K,F) & W_C\sqrt{J(J+1)-K(K-1)} \\ W_C\sqrt{J(J+1)-K(K-1)} & E\left(v_2=1,v_6^l=2^2,J,K-1,F\right) \end{pmatrix}, \tag{3}$$

where $W_C$ is a Coriolis coupling constant. The diagonal elements are nonperturbed vibration-rotation energy represented in usual notation by

$$\begin{aligned} E(v_1=1,J,K,F) = {} & T_{v_1=1} + B_{v_1=1}J(J+1) + \left(A_{v_1=1} - B_{v_1=1}\right)K^2 - D^J_{v_1=1}J^2(J+1)^2 \\ & - D^{JK}_{v_1=1}J(J+1)K^2 - D^K_{v_1=1}K^4 + E^Q_{v_1=1}(I=5/2,J,K,F) \end{aligned} \tag{4}$$

and

$$\begin{aligned} E\left(v_2=1,v_6^l=2^l,J,K,F\right) = {} & T_{v_2=1,v_6=2} + B_{v_2=1,v_6=2}J(J+1) + \left(A_{v_2=1,v_6=2} - B_{v_2=1,v_6=2}\right)K^2 \\ & - 2A_{v_2=1,v_6=2}\zeta_{v_2=1,v_6=2}Kl - D^J_{v_2=1,v_6=2}J^2(J+1)^2 - D^{JK}_{v_2=1,v_6=2}J(J+1)K^2 \\ & - D^K_{v_2=1,v_6=2}K^4 + E^Q_{v_2=1,v_6=2}(I=5/2,J,K,F). \end{aligned} \tag{5}$$

The molecular constants are fixed at the values given by Paso and co-workers [11] in Eqs. (4) and (5) while the quadrupole coupling constants are adjustable parameters in the analysis.

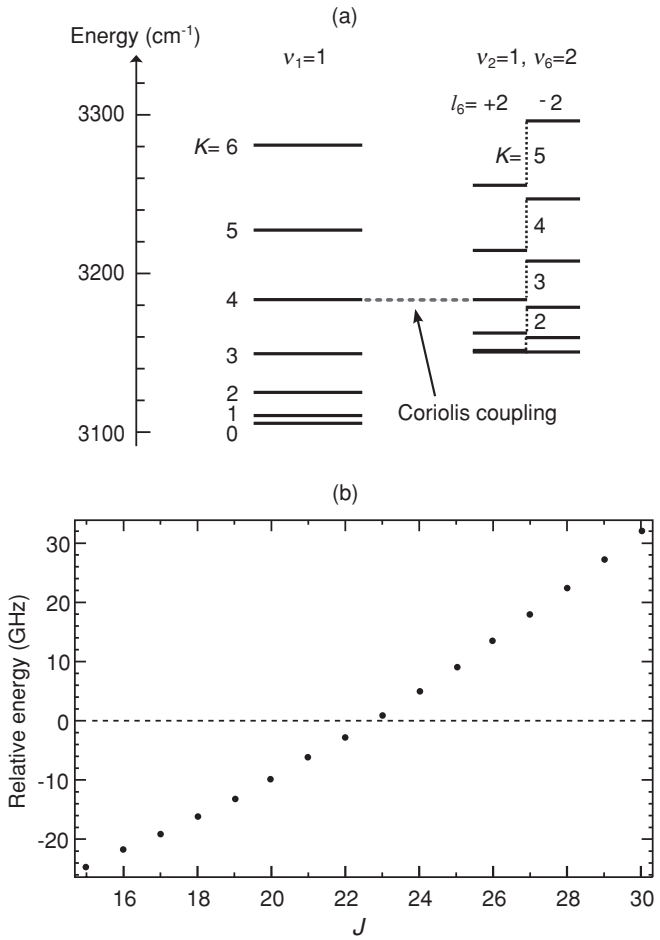


FIG. 3. (a) Energy-level diagram of $CH_3I$ at $J = 23$ to illustrate the energy coincidence between the $v_1 = 1$ and $(v_2, v_6^l) = (1,2^2)$ states [11], and (b) the nonperturbed energy of the $(v_1 = 1, J, K = 4)$ level relative to that of the $(v_2 = 1, v_6^l = 2^2, J, K = 3)$ level.

The observed hyperfine-resolved spectrum of the specific transition is first modified by removing the slope of the baseline and then fit to a sum of six first derivatives of the Lorentz profile with adjustable parameters of six relative frequencies, six relative intensities, and six linewidths by the least-squares method. We thus obtain five frequency intervals between the hyperfine components per transition. Subsequently, the obtained 145 frequency intervals of the 29 transitions are fit by the least-squares method to those calculated from the eigenenergies of the Hamiltonian given by Eq. (3) to yield the three constants, $(eqQ)_{v_1=1}$, $(eqQ)_{v_2=1,v_6=2}$, and $W_C$. Table III lists the determined constants, the standard deviations of the constants, and that of the fit. Figure 5 illustrates the observed spectrum of the $\nu_1$ $P(23,4)$ transition together with the bars recalculated from the obtained constants. The recalculated frequency intervals are also indicated in Table II with the discrepancies. Both indicate excellent agreement between the observations and the recalculations.

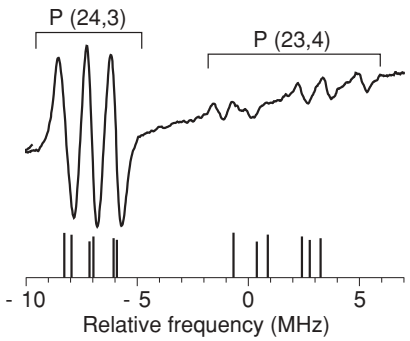


FIG. 4. Observed spectrum of the $\nu_1$ $P(24,3)$ and $P(23,4)$ transitions (upper), and calculated spectrum from the hyperfine coupling constants of the ground and $v_1 = 1$ states [23,24].

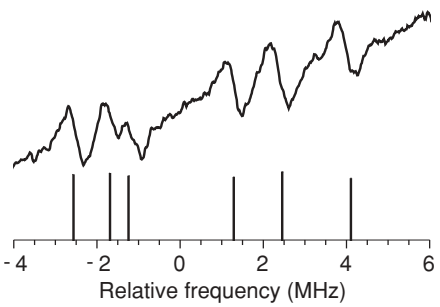


FIG. 5. Observed spectrum of the $\nu_1$ $P(23,4)$ transition (upper) and recalculated spectrum, taking into account the Coriolis interaction (lower).

## V. DISCUSSION

The observed Lamb dip is 250 kHz wide (HWHM) at best, and it is limited by the pressure broadening of 150 kHz at 1.9 Pa [25], the modulation broadening of 30 kHz, the transit-time broadening of 28 kHz for the $1/e^2$-beam radius of 0.71 mm at the beam waist, the spectral linewidth of the DFG source, and the drift of the cavity length. The linewidth of the DFG source is determined by those of the Nd:YAG laser and the ECLD. The former is as narrow as 5 kHz; the latter, whose frequency is stabilized to one of the cavity modes, is estimated as follows. The beat note between the ECLD and the DFB laser [5,7] is observed with a spectrum analyzer, and the linewidth of the beat note is less than 50 kHz. Therefore the linewidth of the stabilized ECLD is less than 50 kHz. The linewidth of the DFB laser is nominally 60 kHz but has not been measured yet. The resolution of the recorded spectrum is also limited by the drift of the cavity length during a data acquisition time, especially for a long averaging time aimed at achieving better sensitivity. The linewidth of the averaged $1f$ signal increases at a rate of about 10 kHz/s. Therefore a frequency sweep based on a reliable frequency reference (e.g., an optical frequency comb), not the cavity length, is strongly desired to enhance the spectral resolution, the *S*/*N* ratio, and the frequency accuracy.

The value of $(eqQ)_{v_1=1}$ in Table III agrees remarkably well with that of the previous work [24], in which seven $\nu_1$ $P(J = 43$–$46, K = 0$–$6)$ transitions were recorded with a spectral resolution of 100 kHz using a 10-GHz tunable 3.39-$\mu$m He-Ne laser. This excellent agreement indicates that the hyperfine coupling constant of the $v_1 = 1$ state has no significant rotational dependence and that the wide tunable range of the present spectrometer increases the number of the observed lines and statistically reduces the uncertainty, even though the spectral resolution is inferior to that of the previous work [24]. The value of $W_C$ is consistent with Ref. [11], and the uncertainty is reduced more than one order of magnitude because of the higher spectral resolution.

The vibrational dependence of the quadrupole hyperfine constant was investigated for several vibrational states in microwave spectroscopy [18,23]. The quadrupole hyperfine constants for the associated vibrational states predict the value of $(eqQ)_{v_2=1,v_6=2}$ as

$$(eqQ)_G + \delta(eqQ)_{v_2=1} + 2\delta(eqQ)_{v_6=1} = -1949.10(91)\ \text{MHz}, \tag{6}$$

$$(eqQ)_G + \delta(eqQ)_{v_2=1} + \delta(eqQ)_{v_6=2} = -1949.13(95)\ \text{MHz}, \tag{7}$$

and

$$(eqQ)_G + \delta(eqQ)_{v_2=1,v_6=1} + \delta(eqQ)_{v_6=1} = -1950.8(16)\ \text{MHz}, \tag{8}$$

where

$$\delta(eqQ)_v = (eqQ)_v - (eqQ)_G. \tag{9}$$

The values of Eqs. (6) and (7) differ from that obtained in the present work beyond the experimental uncertainty, whereas that of Eq. (8) is consistent with the present work.

TABLE III. Determined molecular constants. The numbers in the parentheses are one standard deviation in the unit of the last digit of the constant.

| | This work | Previous works | Refs. |
|---|---|---|---|
| $(eqQ)_{v_1=1}$ (MHz) | −1937.06(5) | −1937.06(3) | [24] |
| $(eqQ)_{v_2=1,v_6=2}$ (MHz) | −1951.24(12) | | |
| $W_C$ (MHz) | 257.6(10) | 261(30) | [11] |
| Standard deviation of the fit: 0.12 MHz | | | |

## VI. CONCLUSION

The 3.4-$\mu$m spectrometer with the DFG source is combined with the cavity-enhanced cell and the ECLD to extend the tunable range and enhance the sensitivity. The performance of the spectrometer is demonstrated by recording the sub-Doppler resolution spectrum of the $\nu_1$ band of $CH_3I$, and the hyperfine-resolved spectral line is 250 kHz wide. The Coriolis interaction between the $v_1 = 1$ and $(v_2, v_6^l) = (1, 2^2)$ states locally perturbs the hyperfine structure, and three molecular constants, the quadrupole coupling constants of the $v_1 = 1$ and $(v_2, v_6^l) = (1, 2^2)$ states and the Coriolis coupling constant, are accurately determined from the observed spectrum. The spectrometer enables us to investigate the detailed energy structures in the vibrational excited states.

## ACKNOWLEDGMENTS

The authors are grateful to C. Ishibashi of Neoark Co. for designing and assembling the cavity-enhanced cell. This work was supported by SENTAN, Japan Science and Technology Agency (JST).

[1] W. Demtröder, *Laser Spectroscopy*, 4th ed. (Springer-Verlag, Berlin, 2008), Vol. 2, Chap. 2.

[2] K. Bielke and R. Schieder, Opt. Commun. **35**, 342 (1980).

[3] G. Magerl, J. M. Frye, W. A. Kreiner, and T. Oka, Appl. Phys. Lett. **42**, 656 (1983).

[4] O. Tadanaga, T. Yanagawa, Y. Nishida, H. Miyazawa, K. Magari, M. Asobe, and H. Suzuki, Appl. Phys. Lett. **88**, 061101 (2006).

[5] M. Abe, K. Takahata, and H. Sasada, Opt. Lett. **34**, 1744 (2009).
[6] P. Maddaloni, G. Gagliardi, P. Malara, and P. De Natale, Appl. Phys. B: Lasers Opt. **80**, 141 (2005).
[7] K. Takahata, T. Kobayashi, H. Sasada, Y. Nakajima, H. Inaba, and F.-L. Hong, Phys. Rev. A **80**, 032518 (2009).
[8] E. D. Black, Am. J. Phys. **69**, 79 (2001).
[9] R. W. P. Drever, J. L. Hall, F. V. Kowalski, J. Hough, G. M. Ford, A. J. Munley, and H. Ward, Appl. Phys. B: Photophys. Laser Chem. **31**, 97 (1983).
[10] E. W. Jones and H. W. Thompson, Proc. R. Soc. London, Ser. A **288**, 50 (1965); R. J. L. Popplewell and H. W. Thompson, Spectrochim. Acta, Part A **25**, 287 (1969).
[11] R. Paso, V.-M. Horneman, and R. Anttila, J. Mol. Spectrosc. **101**, 193 (1983).
[12] R. Paso, R. Anttila, and G. Guelachvili, J. Mol. Spectrosc. **140**, 46 (1990).
[13] Y. Morino and C. Hirose, J. Mol. Spectrosc. **22**, 99 (1967).
[14] D. Boucher, J. Burie, D. Dangoisse, J. Demaison, and A. Dubrulle, Chem. Phys. **29**, 323 (1978).
[15] A. Dubrulle, J. Burie, D. Boucher, F. Herlemont, and J. Demaison, J. Mol. Spectrosc. **88**, 394 (1981).
[16] S. H. Young and S. G. Kukolich, J. Mol. Spectrosc. **114**, 483 (1985).
[17] B. D. Osipov and M. N. Grabois, J. Mol. Spectrosc. **111**, 344 (1985).
[18] E. Arimondo, P. Glorieux, and T. Oka, Phys. Rev. A **17**, 1375 (1978).
[19] A. J. Gray and R. J. Butcher, Proc. R. Soc. London, Ser. A **445**, 543 (1994).
[20] S. Carocci, A. Di Lieto, A. Menciassi, P. Minguzzi, and M. Tonelli, J. Mol. Spectrosc. **175**, 62 (1996).
[21] C. Ishibashi, R. Saneto, and H. Sasada, J. Opt. Soc. Am. B **18**, 1019 (2001).
[22] C. H. Townes and A. L. Schawlow, *Microwave Spectroscopy* (Dover, New York, 1975), Chap. 6.
[23] S. Carocci, A. Di Lieto, A. De Fanis, P. Minguzzi, S. Alanko, and J. Pietila, J. Mol. Spectrosc. **191**, 368 (1998).
[24] J. L. Hall and J. A. Magyar, in *High Resolution Laser Spectroscopy*, edited by K. Shimoda (Springer-Verlag, Berlin, 1976), Chap. 5.
[25] G. Buffa, A. Di Lieto, P. Minguzzi, O. Tarrini, and M. Tonelli, Phys. Rev. A **37**, 3790 (1988).